J. Fluid Mech. (2009), *vol.* 619, *pp.* 127–145.
doi:10.1017/S0022112008004175 Printed in the United Kingdom

Turbulent Rayleigh–Bénard convection in a near-critical fluid by three-dimensional direct numerical simulation

G. ACCARY[1,2]†, P. BONTOUX[2] AND B. ZAPPOLI[3]

[1]Faculté des Sciences et de Génie Informatique, Université Saint-Esprit de Kaslik, B.P. 446 Jounieh, Lebanon

[2]MSNM-GP, UMR 6181 CNRS, Université Paul Cézanne, Technopôle de Château-Gombert, 38 rue Frédéric Joliot-Curie, 13451 Marseille, France

[3]CNES, 18 Avenue Edouard Berlin, 31401 Toulouse, France

(Received 16 October 2007 and in revised form 27 August 2008)

This paper presents state of the art three-dimensional numerical simulations of the Rayleigh–Bénard convection in a supercritical fluid. We consider a fluid slightly above its critical point in a cube-shaped cell heated from below with insulated sidewalls; the thermodynamic equilibrium of the fluid is described by the van der Waals equation of state. The acoustic filtering of the Navier–Stokes equations is revisited to account for the strong stratification of the fluid induced by its high compressibility under the effect of its own weight. The hydrodynamic stability of the fluid is briefly reviewed and we then focus on the convective regime and the transition to turbulence. Direct numerical simulations are carried out using a finite volume method for Rayleigh numbers varying from 10^6 up to 10^8. A spatiotemporal description of the flow is presented from the convection onset until the attainment of a statistically steady state of heat transfer. This description concerns mainly the identification of the vortical structures in the flow, the distribution of the Nusselt numbers on the horizontal isothermal walls, the structure of the temperature field and the global thermal balance of the cavity. We focus on the influence of the strong stratification of the fluid on the penetrability of the convective structures in the core of the cavity and on its global thermal balance. Finally, a comparison with the case of a perfect gas, at the same Rayleigh number, is presented.

1. Introduction

Convection in a fluid close to its gas–liquid critical point (CP) has been a subject of growing interest since the demonstration of the piston-effect (PE), the thermo-acoustic effect responsible for the fast thermal equilibrium observed in such a fluid in the absence of convection. In 1987, under microgravity conditions, Nitsche & Straub observed a fast and homogeneous increase of the temperature inside a spherical cell containing SF_6 slightly above the CP when subjected to a heating impulse. This phenomenon was then explained theoretically (Zappoli *et al.* 1990; Onuki, Hao & Ferrell 1990; Boukari *et al.* 1990) by the well-known critical anomalies, more precisely by the divergence of the thermal expansion coefficient and the vanishing of its

† Email address for correspondence: gilbertaccary@usek.edu.lb

thermal diffusivity when approaching the CP. Indeed, the heating of a cell containing a supercritical fluid (SCF) induces along the heated wall a thin thermal boundary layer in which density shows large variations because of the divergence of the thermal expansion coefficient; this thermal layer expands, compressing adiabatically the rest of the fluid, leading by thermo-acoustic effects (the so-called PE) to a fast and homogeneous heating of the bulk of the cell. Several experiments were carried out subsequently, mainly in microgravity (Guenoun *et al.* 1993; Straub, Eicher & Haupt 1995; Garrabos *et al.* 1998) but also on Earth (Kogan & Meyer, 1998; Zhong & Meyer 1999), and confirmed the existence of the PE.

Since 1996, many experimental and numerical studies have been devoted to the interaction between the PE and natural convection. The Rayleigh–Bénard configuration (bottom heating) has received particular attention (Kogan, Murphy & Meyer 1999; Amiroudine *et al.* 2001; Furukawa & Onuki 2002) because the hydrodynamic stability of the SCF in that case is governed by an interesting and non-common criterion. Owing to the PE, the thermal field exhibits a very specific structure in the vertical direction. A very thin hot thermal boundary layer is formed at the bottom, then a homogeneously heated bulk settles in the core at a lower temperature, and at the top, a cooler boundary layer is formed in order to continuously match the bulk temperature with the colder temperature of the upper wall. A linear analysis, carried out by Gitterman & Steinberg (1970), showed that the hydrodynamic stability of these thermal boundary layers, when subjected to a gravity field, depends on the interaction between two stability criteria which, for a normally compressible fluid, are separately available at very different space scales: on one hand, the classical Rayleigh criterion, derived from the Boussinesq approximation, hence available at small space scales, and on the other hand, the Schwarzschild criterion, usually encountered in atmospheric science, where the stabilizing effect of the hydrostatic pressure becomes appreciable. Because of the divergence of the isothermal compressibility of a SCF, the Schwarzschild criterion becomes available at small space scales; this was proven theoretically (Gitterman & Steinberg 1970; Carlès & Ugurtas 1999), experimentally (Kogan & Meyer 2001), and numerically (Amiroudine *et al.* 2001). Taking advantage of the interaction between those two stability criteria, a numerical study (Accary *et al.* 2005*a*) showed that, in spite of convection onset in the thermal boundary layers according to the classical Rayleigh criterion, a reverse transition to stability through the Schwarzschild one is possible without any external intervention. In our opinion, the hydrodynamic stability of the thermal boundary layers developed in this configuration has been sufficiently studied (Accary *et al.* 2005*b*) and we focus our attention now on the convective regime of the flow. Because of the particular physical properties of the fluid in the vicinity of the CP, the convective regime of the Rayleigh–Bénard problem is turbulent for unusually low intensities of heating ($\sim$mK). In this paper, three-dimensional direct numerical simulations are carried out for Rayleigh numbers varying from 2.68×10^6 up to 160×10^6. For a perfect gas (PG), this range of Rayleigh numbers corresponds to the transition between soft and hard turbulence; however, this is not always the case for the SCF because of its strong stratification induced by its high isothermal compressibility.

In § 2, the problem under consideration is presented. In § 3, the mathematical model is described together with the acoustic filtering of the Navier–Stokes equations. The numerical method is briefly recalled in § 4 and some details of the numerical simulation are mentioned. In § 5, the hydrodynamic stability of the thermal boundary layers is discussed and the convection onset is briefly reviewed. The beginning of the convective regime is presented in § 6. The steady-state turbulent regime and the details of the

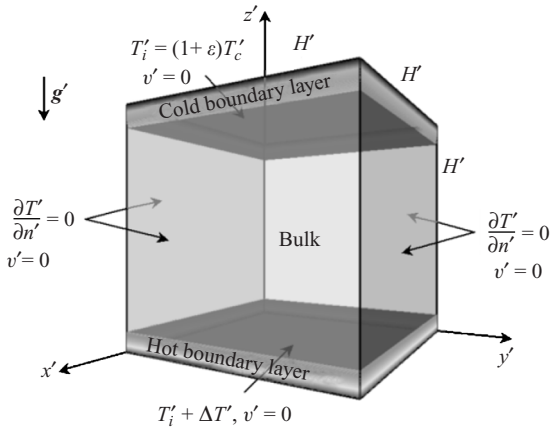

FIGURE 1. Geometry of the cube-shaped cavity and the velocity and temperature conditions applied to the boundaries. The vertical axis z' is co-linear with the acceleration due to the Earth's gravity $\boldsymbol{g}'$. After the first seconds of heating, the temperature field is vertically stratified, divided in three distinct zones: two thermal boundary layers and the bulk of the cavity.

temperature and the dynamic fields are presented in § 7. The global thermal balance of the cavity is discussed in § 8. In § 9, a comparison with the case of a PG is presented at the same Rayleigh number. Finally, the paper is concluded in § 10.

2. The problem under consideration

We consider a SCF in a cube-shaped cavity (of height $H' = 10\,\text{mm}$) subjected to the Earth's gravity field $g' = 9.81\ \text{m s}^{-2}$ (figure 1). The horizontal walls are isothermal while the sidewalls are insulated, and no-slip conditions are applied to all the walls. Initially the fluid is at rest, in thermodynamic equilibrium at a constant temperature T_i' slightly above the critical temperature T_c', such that $T_i' = (1 + \varepsilon)\ T_c'$, where $\varepsilon \ll 1$ defines the non-dimensional proximity to the CP. Under the effect of its own weight, the fluid is stratified in density and in pressure, with a mean density equal to its critical value ρ_c'. While maintaining the top wall at its initial temperature T_i', the temperature of the bottom wall is gradually increased (during 1 s) by $\Delta T'$ (a few mK).

3. The mathematical model

The mathematical model for a SCF flow (Zappoli 1992) is described by the Navier–Stokes and energy equations written for a Newtonian and highly conducting van der Waals fluid:

continuity

$$\frac{\partial \rho'}{\partial t'} + \nabla \cdot (\rho' \boldsymbol{v}') = 0, \tag{1}$$

momentum

$$\frac{\partial (\rho' \boldsymbol{v}')}{\partial t'} + \nabla \cdot (\rho' \boldsymbol{v}' \cdot \boldsymbol{v}') = -\nabla P' + \mu' \left[\nabla^2 \boldsymbol{v}' + \frac{1}{3} \nabla (\nabla \cdot \boldsymbol{v}') \right] + \rho' \boldsymbol{g}', \tag{2}$$

energy

$$\frac{\partial (\rho' e')}{\partial t'} + \nabla \cdot (\rho' e' \boldsymbol{v}') = -P' (\nabla \cdot \boldsymbol{v}') + \nabla \cdot (\lambda' \nabla T') + \Phi', \tag{3}$$

Van der Waals

$$P' + a'\rho'^2 = \frac{\rho' r' T'}{1 - b'\rho'}, \tag{4}$$

where P' is the pressure, T' is the temperature, and ρ' is the density. $\boldsymbol{v}'(u', v', w')$ is the velocity, $\boldsymbol{g}' = (0, 0, -g')$, e' is the internal energy, and Φ' is the viscous energy dissipation. μ' is the dynamic viscosity, λ' is the thermal conductivity, r' is the PG constant, a' and b' are respectively the energy parameter and the co-volume related to the critical coordinates T_c' and ρ_c' by: $b' = 1/(3\rho_c')$ and $a' = 9\, r' T'_c/(8\rho_c')$.

In spite of its simplicity, the van der Waals equation of state contains the required conditions for the existence of the CP and yields a critical divergence as $(T'/T_c' - 1)^{-1}$ of the thermal expansion coefficient β_P', of the isothermal compressibility χ_T', and of the heat capacity at constant pressure C_P'. Note that the real critical exponents, which are the same for all fluids, differ from those obtained from the van der Waals equation of state but it remains a good approximation to carry out qualitative studies. The critical divergence of the thermal conductivity is given by $\lambda' = \lambda_0'(1 + \Lambda\varepsilon^{-0.5})$ where $\Lambda = 0.75$ and λ_0' is the thermal conductivity for a PG. The heat capacity at constant volume C_V' and the dynamic viscosity are supposed to be constant and equal to those of a PG, C_{V0}' and μ_0' respectively. With the van der Waals equation of state, the expression of the internal energy is given by $\delta e' = C_V' \delta T' - a' \delta\rho'$.

In order to make the variables dimensionless, T_c', ρ_c', and $r'\rho_c' T_c'$ are used respectively as representative scales of the thermodynamic variables T', ρ', and P'. The independent variables of length $\boldsymbol{x}'$ (x', y', z') and time t' are scaled respectively by the height of the cavity H' and the PE time scale given by $t_{PE}' = \Psi^{-1}\rho_c' H'^2/\mu_0'$ with $\Psi = \varepsilon^{-1}(\Lambda^{-1} + \varepsilon^{-0.5})$ (Zappoli 1992; Zappoli *et al.* 1999). The PE time scale is the time necessary for the PE to homogenize the temperature in the core of the cavity; it is between the acoustic time scale (H'/c') and the thermal diffusion one (H'^2/D_T') where c' is the sound velocity in the SCF and D_T' is the thermal diffusivity. Hence, the representative scale of velocity is $V_{PE}' = H'/t_{PE}'$. This scaling introduces the Reynolds number $Re = \Psi$, the Froude number $Fr = (V_{PE}')^2/(g'H')$, the Prandtl number based on the properties of the PG assumption, $Pr_0 = \mu_0' C_{P0}'/\lambda_0'$, and the Mach number $Ma = V_{PE}'/c_0'$ where $c_0' = \sqrt{\gamma_0 r' T_c'}$ is the speed of sound for a PG (with $\gamma_0 = C_{P0}'/C_{V0}'$). Note that the PE time scale obtained by Onuki *et al.* (1990) is given by $t_1' = H'^2/D_T'\ (\gamma - 1)^2$, where D_T' is the thermal diffusivity and $\gamma = C_P'/C_V'$ is the specific-heat ratio. Adapted for a van der Waals' gas and with the assumption that $\varepsilon \ll 1$, $t_1' \approx Pr/\Lambda\gamma_0(\gamma_0 - 1) \times t_{PE}'$ (where $\gamma/\gamma_0 = C_P/C_{P0} = 1 + (1 - 1/\gamma_0)\varepsilon^{-1}$).

Despite its high isothermal compressibility, the sound speed c' in a SCF, defined by $c'^2 = C_P'/C_V' \times \chi'_T{}^{-1}$, does not vanish at the CP according to the van der Waals equation of state, indeed C_P'/C_V' and χ_T' diverge with the same critical exponent of -1, which allows the acoustic filtering of the equations. Hence with the basic assumption that $Ma \ll 1$, all the primary dimensionless variables of the problem $\boldsymbol{\phi} = {}^t(\boldsymbol{v}, T, P, \rho)$ can be expanded in series of Ma^2 (Paolucci 1982) as follows: $\boldsymbol{\phi} = \boldsymbol{\phi}^{(0)} + \gamma_0\, Ma^2 \boldsymbol{\phi}^{(1)} + o(Ma^2)$ where $\boldsymbol{\phi}^{(0)}$ and $\boldsymbol{\phi}^{(1)}$ are $O(1)$ The $O(1)$ and $O(Ma^2)$ parts of the governing equations resulting from this expansion that need to be solved are: $O(1)$ continuity

$$\frac{\partial\rho}{\partial t} + \nabla\cdot(\rho\cdot\boldsymbol{v}) = 0, \tag{5}$$

$O(1)$ momentum

$$\nabla P_{th} = 0,$$

$O(Ma^2)$ momentum

$$\frac{\partial(\rho \boldsymbol{v})}{\partial t} + \nabla\cdot(\rho \boldsymbol{v}\boldsymbol{v}) = -\nabla P^{(1)} + \frac{1}{Re}\left[\nabla^2 \boldsymbol{v} + \frac{1}{3}\nabla(\nabla\cdot\boldsymbol{v})\right] + \frac{\boldsymbol{e}_g}{Fr}(\rho - \rho_i), \tag{6}$$

$O(1)$ energy

$$\frac{\partial(\rho T)}{\partial t} + \nabla\cdot(\rho \boldsymbol{v} T) = -(\gamma_0 - 1)(P_{th} + a\rho^2)(\nabla\cdot\boldsymbol{v}) + \frac{\gamma_0}{RePr_0}\nabla\cdot[(1 + \Lambda(T-1)^{-0.5})\nabla T], \tag{7}$$

$O(1)$ van der Waals

$$P_{th} + P_{hyd} = \frac{\rho T}{1 - b\rho} - a\rho^2. \tag{8}$$

In these equations, $\boldsymbol{v}(u, v, w)$, T, P, and ρ refer to the $O(1)$ of the dimensionless variables, the superscript (0) has been omitted for conciseness. P_{th} and P_{hyd} are respectively the thermodynamic pressure (homogeneous in space but time varying according to the $O(1)$ momentum equation) and the time-independent hydrostatic pressure ($P^{(0)} = P_{th} + P_{hyd}$), $a = 9/8$ and $b = 1/3$ are the dimensionless parameters of the van der Waals equation of state, and $\boldsymbol{e}_g = (0,0,-1)$. Before the heating begins, the initial dimensionless density distribution ρ_i, the initial thermodynamic pressure P_{thi}, and the hydrostatic pressure P_{hyd} are obtained from the initial thermodynamic and static equilibrium with the constraint of a dimensionless mean density equal to 1. This results in

$$T_i = 1 + \varepsilon,\ \rho_i = \frac{K}{\mathrm{e}^K - 1}e^{Kz},\ P_{th_i} = \frac{1+\varepsilon}{1-b} - a,\ P_{hyd} = \chi_T^{-1}(\rho_i - 1), \tag{9}$$

where

$$\chi_T^{-1} = \frac{1+\varepsilon}{(1-b)^2} - 2a, \quad K = \chi_T \frac{\gamma_0 Ma^2}{Fr}.$$

This low-Mach-number approximation differs from the classical one where $\rho_i = 1$ and consequently $P_{hyd} = 0$. Indeed, owing to the divergence of the isothermal compressibility of the SCF, the hydrostatic pressure induces density variations $(\rho_i - 1)$ comparable to those resulting from a weak heating. This has been done by keeping the buoyancy term $(\gamma_0 Ma^2/Fr)\rho^{(0)}\boldsymbol{e}_g$ in the leading $O(Ma^2)$ order of the momentum equation (6), while in the classical low-Mach-number approximation this term is shifted to $O(Ma^4)$. It has been shown that this modification is essential for a correct prediction of the convection onset in the thermal boundary layers (Accary *et al.* 2005*c*).

We consider the carbon dioxide critical coordinates ($T_c' = 304.13$ K, $\rho_c' = 467.8$ Kg m^{-3}) and physical properties ($r' = 188$ J Kg^{-1} K^{-1}, $\mu_0' = 3.44 \times 10^{-5}$ Pas, $C_{V0}' = 658$ J Kg^{-1} K^{-1}, $\lambda_0' = 0.01$ W m^{-1} K^{-1}, $Pr_0 = 2.274$). The simulations were carried out for $T_i' - T_c' = 1$ K ($\varepsilon = 3.29 \times 10^{-3}$); in this case, $t_{PE}' = 0.256$ s, $V_{PE}' = 3.9$ cm s^{-1}, $Re = 5710$, $Fr = 1.55 \times 10^{-2}$, $K = (4/9\varepsilon)(\gamma 0 Ma^2/(Fr) = 2.32 \times 10^{-4}$, and the effective Prandtl number $Pr = Pr_0\varepsilon^{-0.5} = 39.6$.

4. Numerical method

The governing equations are solved using a fully implicit finite volume method on a staggered structured but non-uniform mesh using the PISO velocity–pressure coupling algorithm (Patankar 1980). The method is second-order accurate in space: a

second-order hybrid interpolation is used for the advective terms while a second-order central difference scheme is used for the discretization of the diffusion terms. Using a three-level Euler scheme, the method is accurate to the third order in time. The numerical scheme is accurate and stable for a very wide range of the grid Péclet number.

At each time step and at each PISO iteration k, after computing the temperature field, the density is linearized using the van der Waals equation as follows:

$$\rho^k = \frac{P_{th}^k + P_{hyd}}{\dfrac{T^k}{1 - b\rho^{k-1}} - a\rho^{k-1}} = \frac{P_{th}^k + P_{hyd}}{f(T^k, \rho^{k-1})}. \tag{10}$$

The thermodynamic pressure at iteration k is computed from the conservation of the total mass of the fluid, since

$$\int_\Omega \rho^k \mathrm{d}V = 1 = P_{th}^k \int_\Omega \frac{\mathrm{d}V}{f(T^k, \rho^{k-1})} + \int_\Omega \frac{P_{hyd}\,\mathrm{d}V}{f(T^k, \rho^{k-1})}. \tag{11}$$

Then the density field at iteration k is updated using (10). More details about the numerical method can be found in Accary & Raspo (2006) where the code has been thoroughly validated on an analytical solution and on several benchmark problems of natural convection.

The dimensionless computational domain is a cube of unit length, $\Omega = [0,1]^3$. For the momentum equation, Dirichlet conditions ($\boldsymbol{v} = 0$) are applied on all boundaries. For the energy equation, homogeneous Neumann conditions are applied on the vertical boundaries and Dirichlet conditions on the horizontal ones: $T(z=1) = T_i$ and after 1 s of simulation $T(z=0) = T_i + \Delta T$, $\Delta T = \Delta T'/T_c'$ being the dimensionless intensity of heating.

The mesh size and time step depend on the heating applied to the bottom plate; the mesh size varies between 100^3 and 200^3 computation points and the dimensionless time step varies between 0.01 and 0.1. For a better description of the solution in the boundary layers, the mesh is refined in the vicinity of the walls; as one moves away from the wall, the control volume size increases according to a geometric progression of ratio 2. At each time step, the converged solution is supposed to be obtained when the residuals of all transport equations reach 10^{-9} in non-dimensional form.

5. Hydrodynamic stability of the thermal boundary layers

As mentioned earlier, because of the PE, the temperature field is stratified vertically with three distinct zones after the first few seconds of heating: the hot boundary layer, the cold boundary layer and the bulk of the cavity. Regardless of the considered heating, as long as the flow is dominated by the diffusion and by the PE, the thermal boundary layers grow as $\sqrt{D_T' t'}$ with $D_T' = 5.18 \times 10^{-5}$ cm^2 s^{-1}. For $\Delta T' = 1$ mK, figure 2(a) shows the fast and homogeneous increase of the temperature in the bulk of the cavity by the PE and the growth of the thermal boundary layers. Figure 2(b) shows the corresponding density profiles; we notice that the density variations induced by the heating are comparable to those resulting from the hydrostatic pressure, which justifies the adaptation of the low-Mach-number approximation by including the fluid stratification in the model.

The thickness h' of the hot boundary layer is defined as the average distance from the bottom wall to where the local vertical temperature gradient becomes equal to the global one between the horizontal plates, $\Delta T'/H'$. The total temperature variation

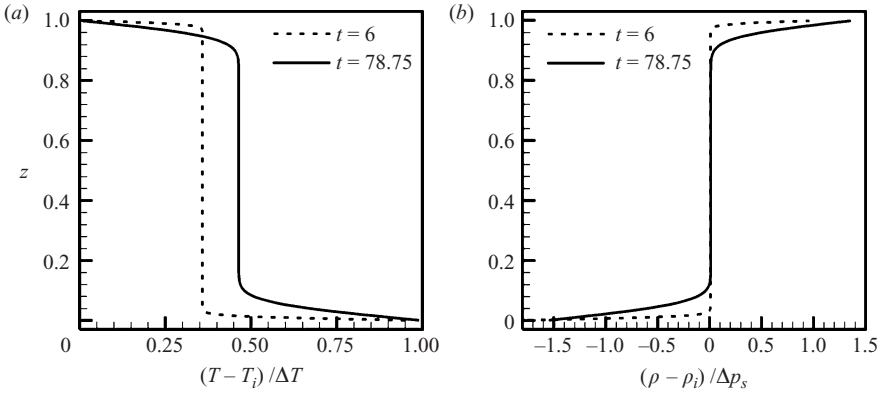

FIGURE 2. (*a*) Temperature profiles for $\Delta T' = 1$ mK showing the action of the PE and the growth of the thermal boundary layers before the convection onset. (*b*) The corresponding density profiles scaled by the density variation due to stratification in the dimensionless form, $\Delta\rho_s = K = (4/9\varepsilon)(\gamma_0 Ma^2/(Fr)$.

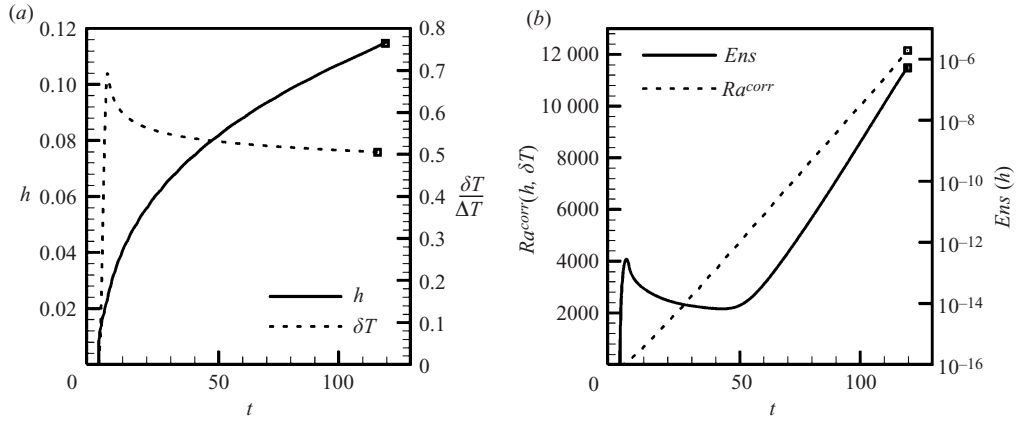

FIGURE 3. (*a*) Time evolution of the hot boundary layer thickness h and of the temperature difference inside it δT for $\Delta T' = 1$ mk. The symbol (□) indicates the beginning of the convective regime. (*b*) Time evolution of the local Rayleigh number $Ra^{corr}(h, \delta T)$ related to the hot boundary layer by (1) and of the mean enstrophy in the hot boundary layer (14) showing the exponential increase of the intensity of convection.

inside the hot boundary layer is denoted $\delta T'$. The normalized variables $h = h'/H'$ and $\delta T = \delta T'/T'_c$ are also defined. For $\Delta T' = 1$ mK, figure 3(*a*) shows the time evolution of h and of δT until the beginning of the convective regime. δT increases to reach a maximum after 1 s of heating, and then it decreases progressively according to the function $e^t \times \mathrm{erfc}(\sqrt{t})$ (Zappoli & Durand-Daubin 1994) as a result of the PE action that increases the temperature of the core. For a SCF diffusing layer, the local Rayleigh number based on h and δT is given by (Gitterman & Steinberg 1970; Carlès & Ugurtas 1999):

$$Ra^{corr}(h, \delta T) = \frac{g' \rho_c'^2 \beta'_P C'_P h'^4}{\lambda' \mu'} \left(\frac{\delta T'}{h'} - \frac{\Delta T'_a}{H'} \right). \tag{12}$$

To account for the high compressibility of the SCF, the classical expression of the Rayleigh number is modified in (12) by the adiabatic temperature gradient

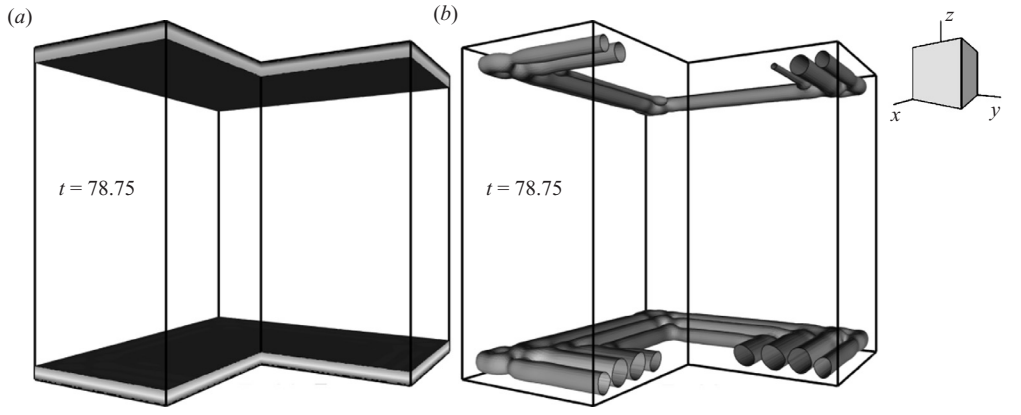

FIGURE 4. (*a*) A cut of the temperature field for $\Delta T = 3\Delta T_a$; the lower and upper shaded isotherms correspond respectively to $(T - T_i)/\Delta T = 0.33$ and 0.66. (*b*) A cut of the iso-surface $Q = 2 \times 10^{-8}$ ($Q_{min} = -1.4 \times 10^{-5}$, $Q_{max} = 2.8 \times 10^{-5}$) shaded by the values of the vertical component w of the velocity showing the vortical structures in the thermal boundary layers shown in (a).

$(\Delta T'_a/H' = g'\beta'_P T'_i/C'_P)$ obtained by moving a fluid particle along the hydrostatic pressure gradient. This term, that can be neglected for a normally compressible fluid, represents the stabilizing contribution of the Schwarzschild criterion commonly encountered for large air columns, and according to which the fluid layer is stable if

$$\frac{\delta T'}{h'} < \frac{\Delta T'_a}{H'} = \frac{g'\beta'_P T'_i}{C'_P}. \tag{13}$$

In the considered model, the adiabatic temperature gradient $\Delta T'_a/H' = 0.34$ mK cm^{-1} and does not depend on the proximity ε to the CP since β'_P and C'_P have the same critical exponent of -1. To better estimate the interaction between natural convection and stratification, the normalized intensity of heating of the bottom wall ΔT is henceforth expressed in terms of $\Delta T_a = \Delta T'_a/T'_c$.

Figure 3(*b*) shows the time evolution of $Ra^{corr}(h, \delta T)$ for $\Delta T = 3\Delta T_a$. According to (12), $Ra^{corr}(h, \delta T)$ behaves as $h^3 \times \delta T \sim t\sqrt{t} \times \mathrm{e}^t \times \mathrm{erfc}(\sqrt{t})$; in fact, $Ra^{corr}(h, \delta T)$ can be very well fitted in figure 3(*b*) by the curve $180 \times t\sqrt{t} \times \mathrm{e}^t \times \mathrm{erfc}(\sqrt{t})$, and we can easily prove that at long time scales, $\mathrm{erfc}(\sqrt{t}) \sim \mathrm{e}^{-t} \times t^{-\frac{1}{2}}$, which explains the linear time evolution of $Ra^{corr}(h, \delta T)$. When the local Rayleigh number exceeds the critical value of about 1100 (Chandrasekar 1961), the hot boundary layer becomes unstable and convective cells start to become organized along the bottom plate. The considered critical Rayleigh number is that of a fluid layer with mixed (solid–free) boundary conditions. However, because the hot boundary layer is connected to the bulk of the cavity, its upper boundary is not sharply defined, and the real critical Rayleigh number should slightly differ from 1100; but this value, even though not precise, remains the most suitable theoretical value for the considered configuration. Figure 4(*b*) enables the visualization of these vortical structures along the isothermal walls using the Q-criterion given by $Q = \frac{1}{2}(\Omega_{ij}\Omega_{ij} - S_{ij}S_{ij})$ where S_{ij} and Ω_{ij} denote respectively the symmetric and anti-symmetric parts of $\nabla \boldsymbol{v}$. (Dubief & Delcayre 2000). Then, the intensity of these vortices rises exponentially with time; this can be easily seen on the time evolution of the mean enstrophy in the hot boundary layer shown

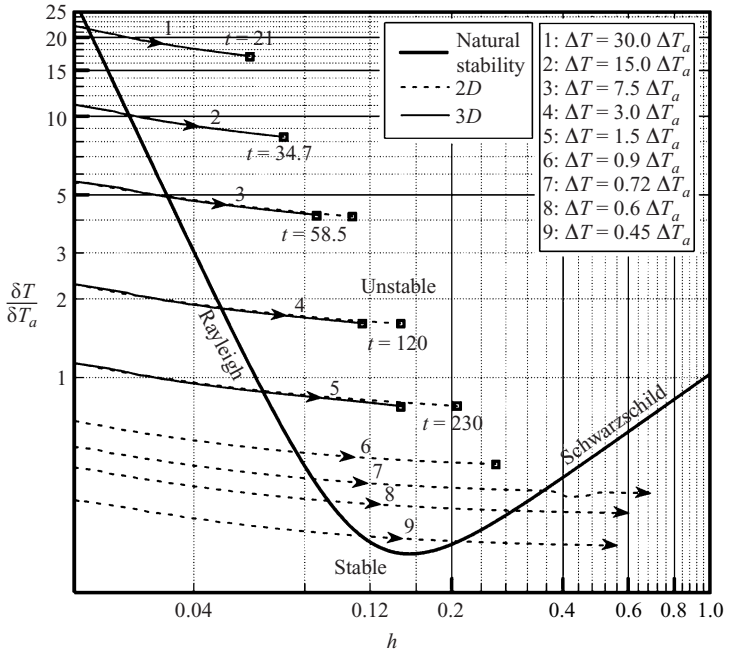

FIGURE 5. Evolution of the temperature difference δT across the hot boundary layer as a function of its thickness h. Time evolves in the arrows' direction and the symbols (□) correspond to the beginning of the convective regime. The neutral stability line was derived from (12). The two-dimensional results were obtained using a cavity of height 1.5 H′ with periodic vertical boundaries; for $\Delta T \leqslant 0.72\Delta T_a$, a reverse transition to stability is obtained though the Schwarzschild line.

in figure 3(*b*) and defined by

$$Ens(h) = \frac{1}{2h}\int_0^h \left[\left(\frac{\partial u}{\partial y} - \frac{\partial v}{\partial x}\right)^2 + \left(\frac{\partial u}{\partial z} - \frac{\partial w}{\partial x}\right)^2 + \left(\frac{\partial v}{\partial z} - \frac{\partial w}{\partial y}\right)^2\right] \mathrm{d}z. \qquad (14)$$

The intensity of these convective cells keeps rising until they produce enough convective transport to deform the isotherms causing the collapse of the thermal boundary layers. For $\Delta T = 3\Delta T_a$, the collapse of the hot boundary layer occurs around $t = 120$ and corresponds to the symbol (□) in figures 3(*a*) and 3(*b*); afterwards the convective regime starts and the definition of the hot boundary layer holds no more. The cold boundary layer developed along the top plate is governed by the same mechanisms and its hydrodynamic stability depends on the same criterion (Accary *et al.* 2005*b*); the same scenario occurs for the cold boundary layer.

In figure 5, the critical value of δT for the convection onset in the hot boundary layer is derived from (12) and plotted versus h (the thick solid line) defining the unstable zone. This neutral stability curve consists of two lines representing the limits of the convection-onset criterion depending on h. For small values of h, the fluid compressibility can be neglected and the stability of the hot boundary layer is governed by the classical Rayleigh criterion, obtained from (12) by dropping the term $g'\beta'_P T'_i/C'_P$, while for larger values of h, viscosity and thermal diffusion are neglected, and the stability depends on the Schwarzschild criterion obtained from (13). For several intensities of heating ΔT, figure 5 shows the evolution curves

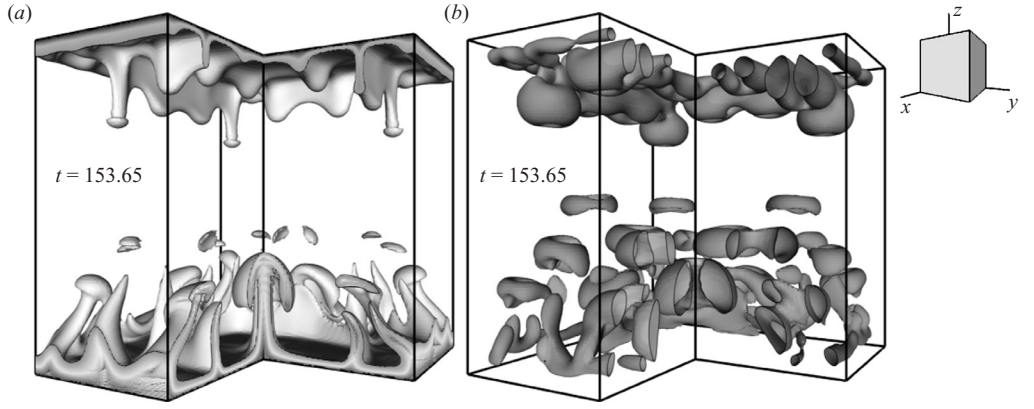

FIGURE 6. (*a*) A cut of the temperature field for $\Delta T = 3\Delta T_a$ showing the beginning of the convective regime; the lower and upper shaded isotherms correspond respectively to $(T - T_i)/\Delta T = 0.33$ and 0.66. (*b*) A cut of the corresponding iso-surface $Q = 0.015$ ($Q_{min} = -0.15$, $Q_{max} = 0.15$).

$\delta T(h)$ for the hot boundary layer until the beginning of the convective regime, which corresponds to the symbol (□). Figure 5 also shows results obtained in a two-dimensional approximation with periodic vertical boundaries (the dashed lines) (Accary *et al.* 2005*c*). The boundary effects induced by the presence of the lateral walls in the three-dimensional case accelerates the development of convection and, at equal intensity of heating, the convective regime is reached earlier in comparison with the two-dimensional approximation with periodic vertical boundaries. For low intensities of heating, in practice for $\Delta T \leqslant 0.72\Delta T_a$, once the hot boundary layer has become unstable, the intensity of the convective cells rises exponentially with time until they deform the isotherms. However, this deformation is not large enough to induce the collapse of the hot boundary layer that keeps growing and the curve $\delta T(h)$ crosses the Schwarzschild line back into the stable zone again and a reverse transition to stability obtained without any external intervention (Accary *et al.* 2005*a*). This phenomenon requires that the thermal boundary layers grow enough without reaching the centre of the cavity (in order to avoid their interaction); a height of *1.5H'* has been necessary in our case.

6. The beginning of the convective regime

The convective regime starts with several plumes rising from within the thermal boundary layers as shown in figure 6(*a*). These plumes are encircled by doughnut-shaped structures shown by the *Q*-criterion in figure 6(*b*). Convection improves the heat transfer between the isothermal walls and the bulk of the cavity, resulting into a faster thermal balance in the whole fluid volume.

For all the heating cases that we considered, the hot boundary layer always became unstable before the cold one. As the heating increases, convection is triggered earlier since the instability criterion ($Ra^{corr}(h, \delta T) > 1100$) is satisfied earlier; consequently, the thickness of the thermal boundary layer is smaller when the convection arises and the size of the convective structures decreases as shown in figure 7. A detailed study of the size of the convective structures has been done in a two-dimensional approximation in Accary *et al.* (2005*b*).

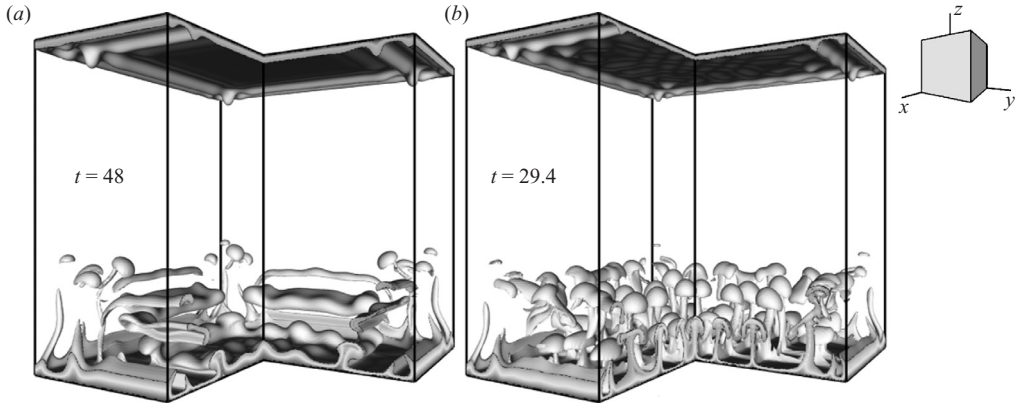

FIGURE 7. Cuts of temperature fields for (*a*) $\Delta T = 15\Delta T_a$ and (*b*) $\Delta T = 30\Delta T_a$ showing the effect of the intensity of heating on the temperature field at the beginning of the convective regime. The lower and upper shaded isotherms correspond respectively to $(T - T_i)/\Delta T = 0.33$ and 0.66.

7. Transition to turbulence

In the convective regime of the flow that follows the convection onset, the Rayleigh number, based on the total height H' of the cavity and on the temperature difference $\Delta T'$ between the isothermal walls, (15), becomes a better indicator of the regime of the flow:

$$Ra^{corr} = \frac{g'\rho_c'^2\beta_P' C_P' H'^4}{\lambda'\mu'}\left(\frac{\Delta T'}{H'} - \frac{\Delta T_a'}{H'}\right). \tag{15}$$

For $\Delta T < \Delta T_a$, the Rayleigh number obtained from (15) is negative; this, however, does not prevent convection arising in the thermal boundary layers when the local Rayleigh number (12) exceeds 1100. But for $\Delta T > \Delta T_a$, for example for $\Delta T = 1.5\Delta T_a$, the term in front of the parentheses in (15), which diverges as $\varepsilon^{-1.5}$, is very large and results in a Rayleigh number of 2.68×10^6, while for a PG the Rayleigh number is directly proportional to ΔT.

The turbulent Rayleigh–Bénard convection is characterized by a statistically steady state of heat transfer. In the considered configuration, the setting in the turbulent regime may be identified from the time evolution of the mean Nusselt numbers on the isothermal walls, given by

$$Nu = -\frac{1}{\Delta T}\frac{\partial T}{\partial z}. \tag{16}$$

For $\Delta T = 7.5\Delta T_a$ which corresponds to $Ra^{corr} = 80\times10^6$, (15), figure 8 shows the time evolution of the mean Nusselt numbers on the bottom wall and on the top one. The convection onset is easily identified by the improvement of the heat transfer corresponding to the increase in the mean Nusselt numbers that afterwards stabilize around almost the same value, which indicates the setting in of the turbulent flow.

Figure 9(*a*) shows the temperature field obtained in the turbulent regime. We notice first the appearance of crest-like patterns defining flat regions on the isothermal walls where the temperature is almost homogeneous in the (x, y) plane, we notice also the spreading of the isotherms along the adiabatic walls. Figure 9(*b*) shows the chaotic flow that takes place in the turbulent regime. The vortical structures have no

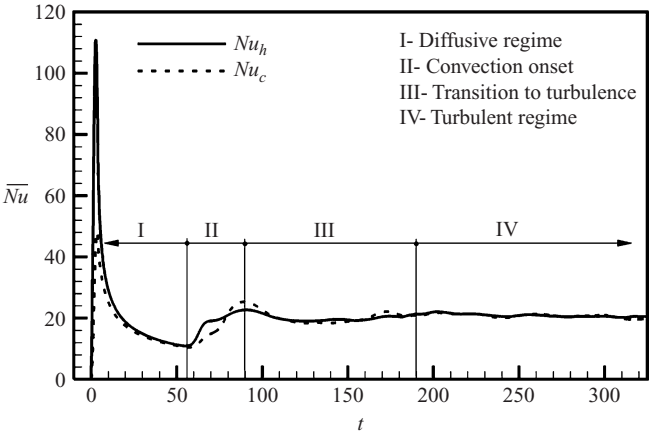

FIGURE 8. Time evolution of the mean Nusselt numbers, (16), on the bottom wall (Nu_h, h for hot) and the top one (Nu_c, c for cold) for $\Delta T = 7.5\Delta T_a$ ($Ra^{corr} = 80 \times 10^6$).

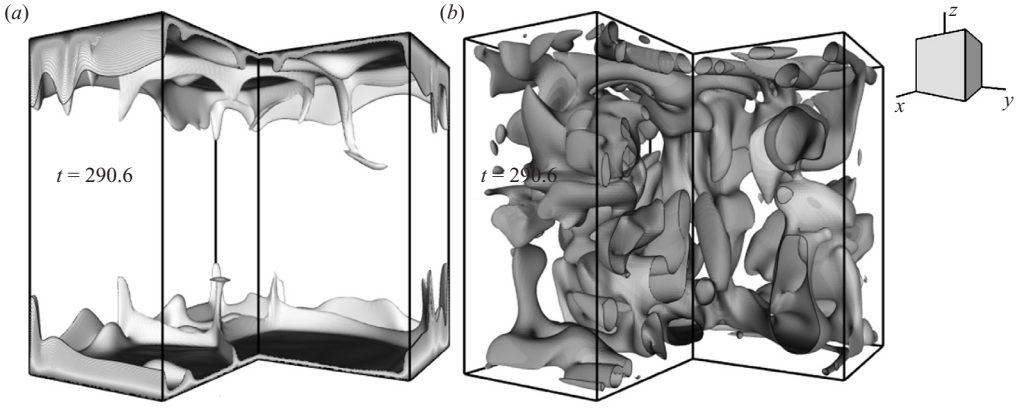

FIGURE 9. (*a*) A cut of the temperature field for $\Delta T = 7.5\Delta T_a$; the lower and upper shaded isotherms correspond respectively to $(T - T_i)/\Delta T = 0.33$ and 0.66. (*b*) A cut of the corresponding iso-surface $Q = 0.015$ ($Q_{min} = -0.37$, $Q_{max} = 0.67$).

particular shape; the tubular and toroidal structures obtained at the beginning of the convective flow have completely disappeared.

In order to better estimate the size of the vortical structures and its time evolution, a discrete Fourier transformation of the vertical velocity component w has been carried out in both the x and y directions. The operation required the fictional assumption of a periodic and odd distribution of w in the horizontal directions with a period of $2H'$. Along the line ($y = y_0$, $z = z_0$) and for a wavelength H'/k associated with the mode k, the Fourier coefficient of $w(x, y_0, z_0)$ is given by

$$W_x(k, y_0, z_0) = \int_0^1 [w(x, y_0, z_0) - (-1)^k w(1 - x, y_0, z_0)]\sin(2\pi kx)\mathrm{d}x. \qquad (17)$$

Once the coefficients $W_x(k, y_0, z_0)$ are computed for all (y_0, z_0), the mean contribution of the mode k to the field of w is determined by

$$\bar{W}_x(k) = \int_0^1 \int_0^1 |W_x(k, y, z)|\mathrm{d}y\mathrm{d}z. \qquad (18)$$

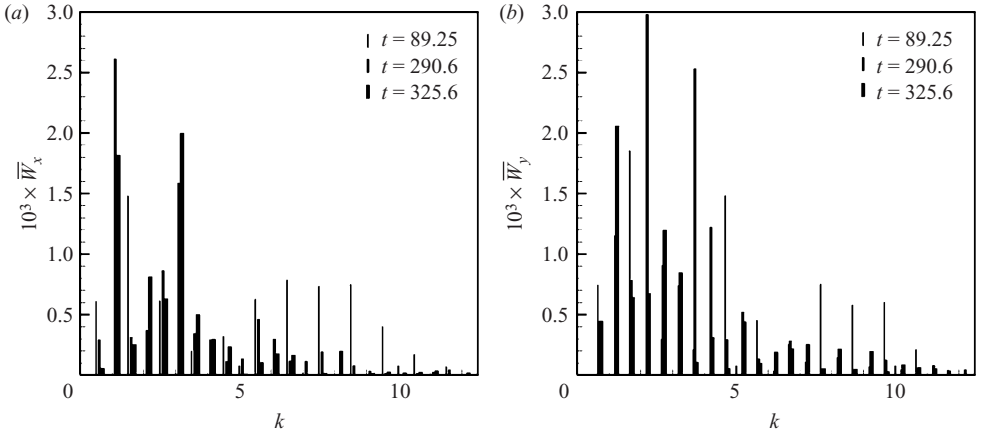

FIGURE 10. The weights of the different wavevectors k in the spectrum of the vertical velocity component w, in the directions x (a) and y (b). On average, the convective structures are clearly larger in the steady-state turbulent regime ($t = 290.6$ and 325.6) than at the beginning of convection ($t = 89.25$).

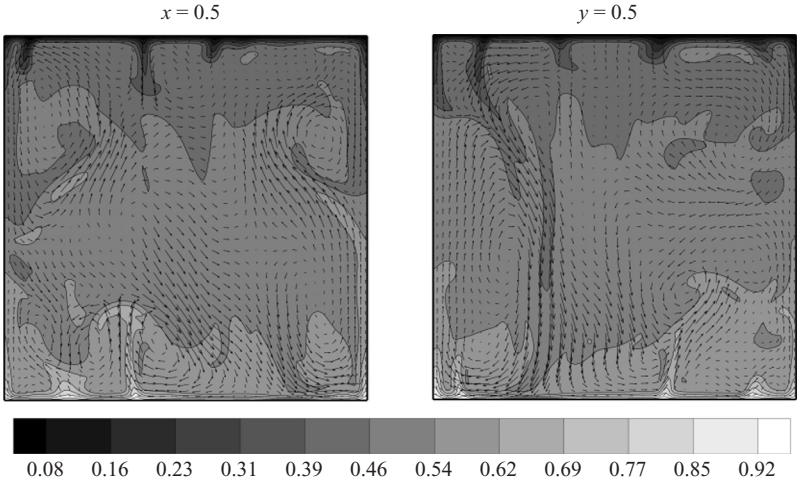

FIGURE 11. Vertical cuts at $x = 0.5$ and $y = 0.5$ of the normalized temperature field $(T - T_i)/\Delta T$ shown in figure 9(a) ($\Delta T = 7.5\Delta T_a$, $t = 290.6$), with the corresponding velocity fields.

Figure 10 shows the contribution of the different modes to the spectrum of the component w in the x and y directions at the beginning of the convective regime and in the turbulent one. We notice an important contribution of small wavelengths ranging between $H'/11$ and $H'/4$ at the beginning of convection (at $t = 89.25$, see figure 8). But as time goes on, the spectra of w show a much higher contribution of large wavelengths, sometimes exceeding half the of the cavity width. Similar results were obtained for the horizontal velocity components, u and v. Thus, the turbulent flow consists mainly of large vortical structures.

Figure 11 shows cuts of the temperature field in the vertical median planes of the cavity with the corresponding velocity fields that confirm the presence of large convective structures in the steady-state turbulent regime. We notice that the temperature field consists mainly of two unstable thermal boundary layers exchanging

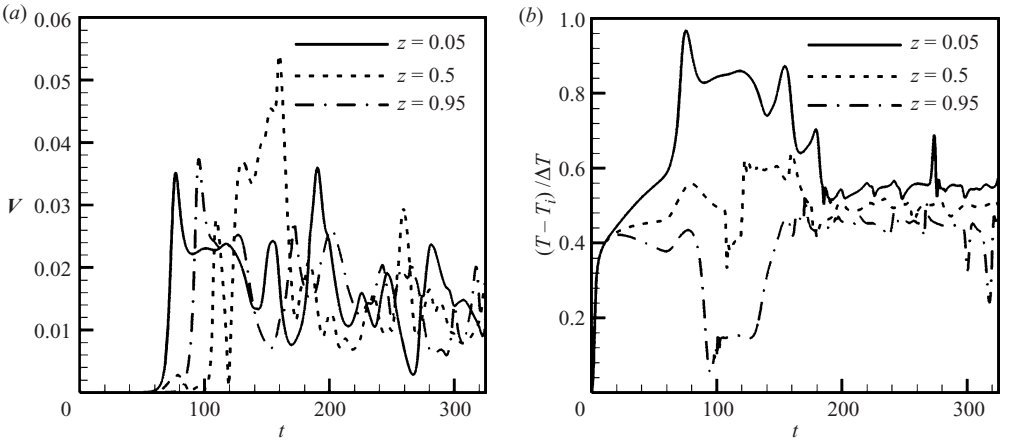

FIGURE 12. Time evolution of (a) the local velocity magnitude (scaled by $V'_{PE} = H'/t'_{PE} = 3.9\,\mathrm{cm\,s^{-1}}$) and ($b$) the local normalized temperature at three positions ($z = 0.05$, 0.5, and 0.95) along the line $x = y = 0.5$, for $\Delta T = 7.5\Delta T_a$.

heat and mass with the bulk of the cavity in which the convective activity induces a quasi-homogeneous temperature.

Figure 12 shows the time evolution, along the vertical axis of the cavity ($x = y = 0.5$), of the velocity magnitude and of the temperature at the free boundaries of the thermal layers ($z = 0.05$ and $z = 0.95$) and at the centre of the cavity; the velocity components have the same order of magnitude. Despite convection, the thickness of the thermal boundary layers may be computed at each point of the horizontal walls using the definition of § 3; the normalized values of the thermal boundary layer thicknesses (averaged in space and in time) are around 0.05. Figure 12(a) underlines the chaotic convection that takes place in the whole fluid volume; the velocity has been monitored at 25 different points of the cavity and confirms the chaotic behaviour. In the steady-state turbulent regime, figure 12(b) shows a slight difference of the time-averaged temperature between positions $z = 0.05$ and $z = 0.95$, which reveals the existence of a temperature gradient in the bulk of the cavity that will be investigated in § 8.

8. The global thermal balance of the cavity

The steadiness of the mean Nusselt numbers on the isothermal walls (figure 8, turbulent regime) reflects the setting in of a statistically steady-state heat transfer across the cavity. However, figure 13 revels the strong non-uniformity of the Nusselt number distributions on the isothermal walls. Of course, these patterns are directly related to those of the temperature field: the Nusselt number minima are reached under the crest-like patterns shown in figure 9(a), while the maxima are obtained inside the cells determined by those patterns. These cells are thus characterized by very thin thermal boundary layers; for the temperature field shown in figure 9(a), the minimal normalized thicknesses of the thermal boundary layer were about 0.014 for the hot boundary layer and 0.012 for the cold one and were obtained where the distributions of the Nusselt numbers reach their maxima.

Despite the strongly non-uniform distributions of the Nusselt numbers, in the steady-state turbulent regime, the mean Nusselt numbers on both isothermal walls fluctuate around the same value. For different intensities of heating and hence Rayleigh

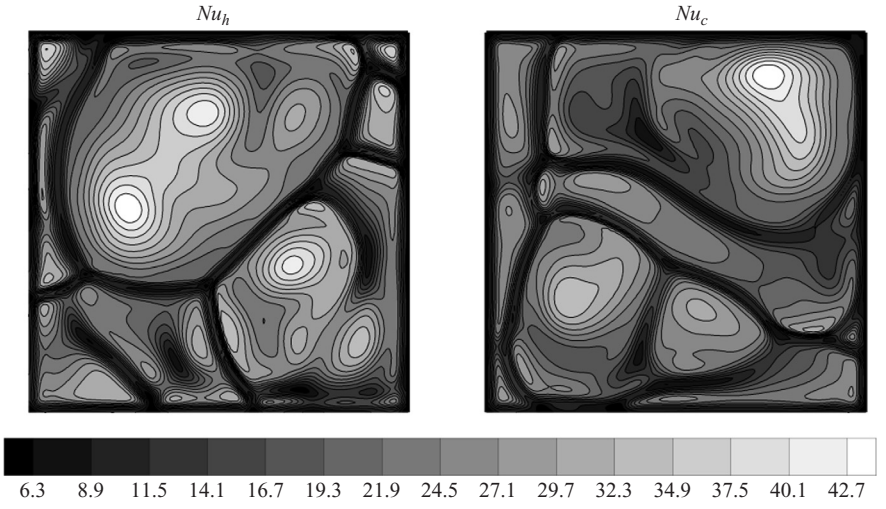

FIGURE 13. Distributions of the Nusselt number on the bottom (Nu_h) and the top (Nu_c) isothermal walls, corresponding to the temperature field shown in figure 9(a) ($\Delta T = 7.5\Delta T_a$, $t = 290.6$).

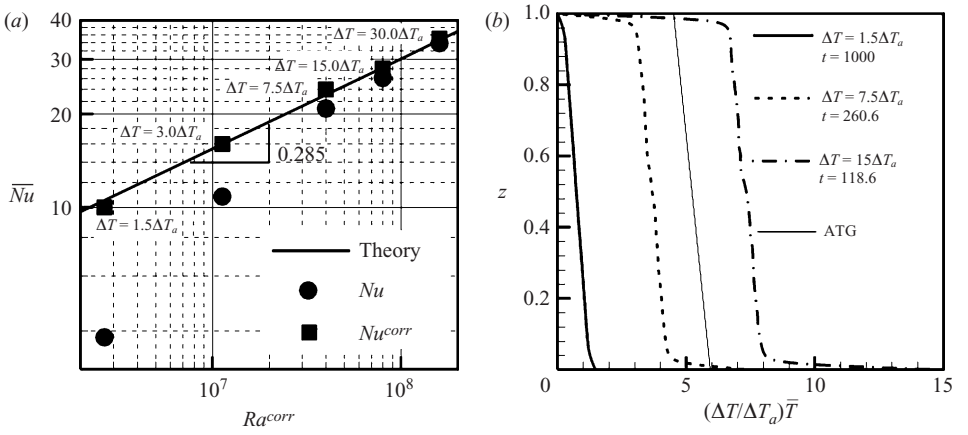

FIGURE 14. In the steady-state regime of the turbulent flow: (a) the classical, (16), and the corrected, (19), mean Nusselt numbers versus the corrected Rayleigh number (15); (b) temperature profiles (averaged on the x, y-plane) for different intensities of heating ($\overline{T}$ varies between 0 and 1), ATG stands for 'adiabatic temperature gradient'.

numbers, figure 14(a) reports the mean Nusselt numbers (the filled circles). For a PG, the experimental results (Poche *et al.* 2004) and those from a scaling theory (Siggia 1994) show that the Nusselt number behaves as $Ra^{2/7}$. This behaviour can be observed for the Nusselt number corrected by the adiabatic temperature gradient (Kogan & Meyer 2001), given by

$$Nu^{corr} = \frac{-\partial T/\partial z - \Delta T_a}{\Delta T - \Delta T_a} = \frac{\Delta T}{\Delta T - \Delta T_a}\left(Nu - \frac{\Delta T_a}{\Delta T}\right). \tag{19}$$

For $\Delta T \gg \Delta T_a$, $Nu^{corr} \to Nu$; but as the intensity of heating decreases, the corrected expression for the Nusselt number (the filled squares in figure 14a) enables the retrieval

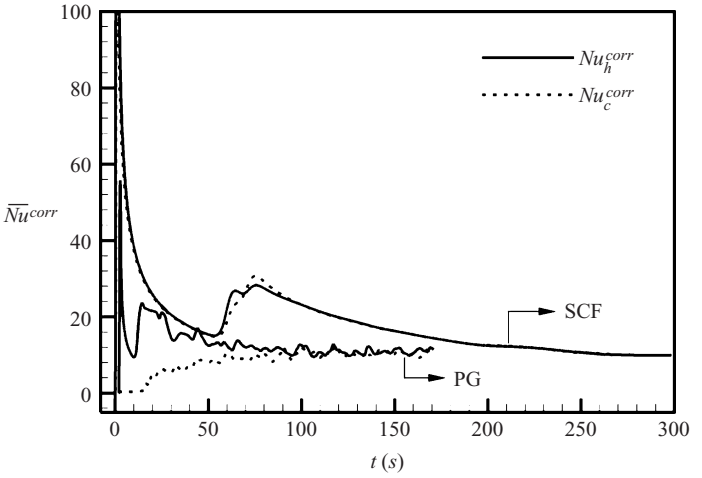

FIGURE 15. Time evolution of the mean Nusselt numbers on the isothermal walls obtained in the three-dimensional case for a Rayleigh number of 2.68×10^6 for a SCF ($\Delta T = 1.5\Delta T_a$) and for a PG. The curves were shifted by 2 s for the PG to show the first peak prominently. For the SCF, the first peak of the mean Nusselt number on the bottom wall reaches the value of 370, and the beginning of convection at about 60 s is consistent with the result shown in figure 5, where the convective regime starts at $t' = 120 \times t_{PE} = 58.9$ s.

of the $Ra^{2/7}$ law. However, it should be recalled that the effective heat transfer is described by the classical expression for the Nusselt number given by (16), not by the corrected one.

At the global thermal balance of the cavity and for all intensities of heating, figure 14(*b*) revels the existence of a mean temperature gradient in the bulk of the cavity equal to the adiabatic temperature gradient. This is a natural structure of the mean temperature field that ensures the minimal temperature gradients in the thermal boundary layers with the constraint of a globally stable bulk of the cavity. Indeed, if the mean temperature gradient in the bulk of the cavity were larger than the adiabatic temperature gradient, the bulk of the cavity would lose its hydrodynamic stability. In return, if the mean temperature gradient in the bulk of the cavity were smaller than the adiabatic temperature gradient, the bulk of the cavity would be 'too' stable, but this would increase the temperature gradients in the thermal boundary layers.

9. Comparison between a SCF and a PG, effects of stratification

A comparison between the Rayleigh–Bénard convection in a SCF and that in a PG is carried out here in the three-dimensional case for a Rayleigh number of 2.68×10^6 for which the density stratification of the SCF clearly affects the development of convection ($\Delta T = 1.5\Delta T_a$). The mathematical model described in § 3 was adapted to the PG case, mainly by setting $a = b = 0$, $\Lambda = 0$, and $\varepsilon = 0$ in (5) to (9), and by choosing reference values of temperature and density compatible with the PG assumption; these were set to 300 K and $1.8\,\mathrm{Kg\,m^{-3}}$ respectively. An intensity of heating of $\Delta T' = 5$ K was applied to the bottom wall in the PG case and the height H' of the cavity, deduced from the classical expression of the Rayleigh number, is equal to 13.8 cm. A mesh of 100^3 and a time step of 0.125 s have been used.

Figure 15 shows the time evolution of the mean Nusselt numbers for the SCF and for the PG. Time is not scaled in this case because the PE does not exist for

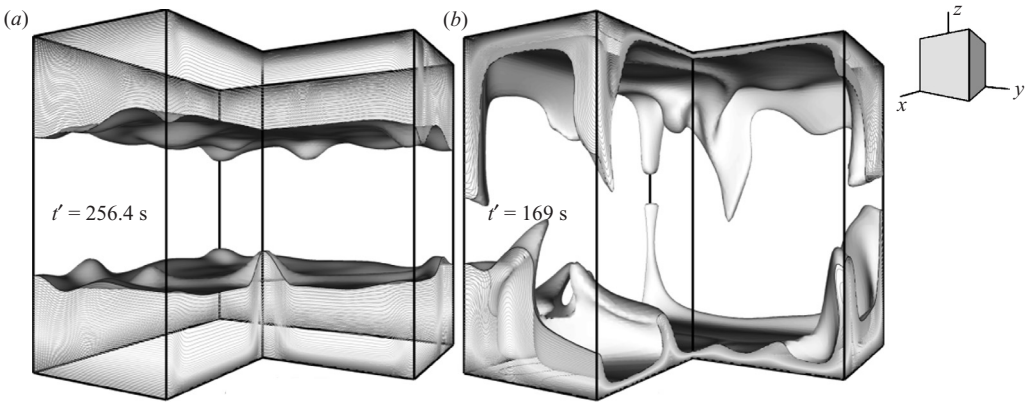

FIGURE 16. Cuts of temperature fields for a Rayleigh number of 2.68×10^6: (*a*) for a SCF ($\Delta T = 1.5\Delta T_a$) and (*b*) for a PG, showing how the strong stratification of the SCF holds back the development of convection. The lower and upper shaded isotherms correspond respectively to $(T - T_i)/\Delta T = 0.33$ and 0.66.

the PG. The adiabatic temperature gradient in a PG is very small compared to $\Delta T'/H'$, hence: $Nu^{corr} \rightarrow Nu$). The large temperature gradients obtained at the very first seconds of heating in the case of the SCF are responsible for the very high peak of the Nusselt number. For the SCF, figure 15 reports very similar evolutions of the mean Nusselt numbers on both isothermal walls. By contrast, for the PG, while the mean Nusselt number on the bottom wall shows a similar behaviour to that of the SCF during the diffusive regime, no heat transfer is detected on the top wall ($Nu_c = 0$) until the beginning of convection. Because the PE is practically non-existent for the PG, the heat transfer is only activated on the top wall when the thermal plumes rising from the hot boundary layer reach it. Even though the Prandtl number is about 18 times smaller (according to the mathematical model, the Prandtl number of the PG is about 2.27 against 39.6 for the SCF), convection in the PG is much more developed than in the SCF at the same Rayleigh number (Verzicco & Camussi 1999), as shown by figure 16. The fluctuating time evolution of the mean Nusselt numbers for the PG results from this intense convective activity. By contrast, the trace of the diffusion-dominated temperature field (figure 16*a*) obtained for SCF due to its strong stratification is visible on the time evolution of the mean Nusselt numbers after the convection onset. Under these conditions, the global thermal balance of the cavity is mainly achieved by diffusion at long time scales because of the critical vanishing (as $\varepsilon^{1/2}$) of the thermal diffusivity of the SCF. We notice finally that even though the temperature field of the SCF is diffusion-dominated while it is convection-dominated for the PG, the corrected mean Nusselt number at the global thermal balance of the cavity is the same in both cases.

10. Conclusions

The numerical simulation of the turbulent Rayleigh–Bénard convection in a SCF is a natural extension of the previous two-dimensional numerical studies of laminar convection and instability mechanisms. In this paper, the mathematical model for SCF flows with the appropriate acoustic filtering has been recalled, then a description of the different stages of the SCF flow in a cube-shaped cavity heated from below were reported from the first seconds of heating until the setting in of a statistically steady state

of heat transfer, for Rayleigh numbers ranging from 2.68×10^6 up to 160×10^6. While the scenarios of the convection onset and disappearance (reverse transition to stability) could be observed in the previously reported two-dimensional results, the convective regime and the transition to turbulence required three-dimensional simulations.

At the beginning of convection, tubular convective structures appear inside the thermal boundary layers while the thermal plumes are encircled by toroidal vortical structures; the size of these structures decreases as the intensity of heating increases. In the turbulent regime, the convective structures grow until their size exceeds half of the cavity, and create on the isothermal walls several cells where an intense heat transfer takes place. Despite the non-homogeneous heat transfer on the isothermal walls, the steadiness of the mean Nusselt numbers around the same value reflects the global thermal balance of the cavity. The relation between that equilibrium Nusselt number and the Rayleigh number obtained for a PG ($Nu \sim Ra^{2/7}$) is applicable to the SCF, provided that the adiabatic temperature gradient is taken into account in the expressions for both numbers. In the turbulent regime, the temperature field consists mainly of two unstable thermal boundary layers and a bulk characterized by a mean temperature gradient equal to the adiabatic temperature gradient. For relatively high intensities of heating ($\Delta T \gg \Delta T_a$), the global thermal balance of the cavity is achieved by a chaotic convection invading in the whole fluid volume. By contrast for weak intensities of heating ($\Delta T \gtrsim \Delta T_a$), the strong density stratification, due to the high isothermal compressibility of the fluid, prevents the free development of convection whose penetrability is dramatically reduced; in this case, the thermal balance of the cavity is mainly achieved by diffusion and therefore on long time scales.

Finally, a comparison between the SCF and the PG for the same Rayleigh number showed two major differences. The first, related to the PE, is the absence of heat transfer on the top wall for the PG until the beginning of convection; while for the SCF, the time evolutions of the mean Nusselt numbers on both isothermal walls are similar. The second, related to the stratification of the SCF and thus only encountered for $\Delta T \gtrsim \Delta T_a$, is the diffusion-dominated thermal balance of the cavity for the SCF, while it is convection-dominated for PG.

The authors thank the financial support of the CNES (Centre National d'Etudes Spatiales) and the computation resources provided by IDRIS (Institut du Developpement et des Ressources en Informatique Scientifique). Scientific and style improvements have been brought to the paper during the review and editing processes.

REFERENCES

Accary, G. & Raspo, I. 2006 A 3D finite volume method for the prediction of a supercritical fluid buoyant flow in a differentially heated cavity. *Comp. Fluids* **35**(10), 1316.

Accary, G., Raspo, I., Bontoux, P. & Zappoli, B. 2005*a* Reverse transition to hydrodynamic stability through the Schwarzschild line in a supercritical fluid layer. *Phys. Rev.* E **72**, 035301.

Accary, G., Raspo, I., Bontoux, P. & Zappoli, B. 2005*b* Stability of a supercritical fluid diffusing layer with mixed boundary conditions. *Phys. of Fluids* **17**, 104105.

Accary, G., Raspo, I., Bontoux, P. & Zappoli, B. 2005*c* An adaptation of the low Mach number approximation for supercritical fluid buoyant flows. *C. R. Méc.* **333**, 397.

Amiroudine, S., Bontoux, P., Larroudé, P., Gilly, B. & Zappoli, B. 2001 Direct numerical simulation of instabilities in a two-dimensional near-critical fluid layer heated from below. *J. Fluid Mech.* **442**, 119.

Boukari, H., Schaumeyer, J. N., Briggs, M. E. & Gammon, R. W. 1990 Critical speeding up in pure fluids. *Phys. Rev.* A **41**, 2260.

Carlès, P. & Ugurtas, B. 1999 The onset of free convection near the liquid-vapour critical point. Part I: Stationary initial state. *Physica* D **162**, 69.

Chandrasekar, S. 1961 *Hydrodynamic and Hydromagnetic Stability*. Clarendon.

Dubief, Y. & Delcayre, F. 2000 On coherent-vortex identification in turbulence. *J. Turbulence* **1**, 011.

Furukawa, A. & Onuki, A. 2002 Convective heat transport in compressible fluids. *Phys. Rev.* E **66**, 016302.

Garrabos, Y., Bonetti, M., Beysens, D., Perrot, F., Fröhlich, T., Carlès, P. & Zappoli B. 1998 Relaxation of a supercritical fluid after a heat pulse in the absence of gravity effects: Theory and experiments. *Phys. Rev.* E **57**, 5665.

Gitterman, M. & Steinberg, V. A. 1970 Criteria for the commencement of convection in a liquid close to the critical point. *High Temperature USSR* **8**(4), 754.

Guenoun, P., Khalil, B., Beysens, D., Garrabos, Y., Kammoun, F., Le Neindre, B. & Zappoli B. 1993 Thermal cycle around the critical point of carbon dioxide under reduced gravity. *Phys. Rev.* E **47**, 1531.

Kogan, A. B. & Meyer, H. 1998 Density response and equilibration in a pure fluid near the critical point: ^{3}He. *J. Low Temp. Phys.* **112**, 417.

Kogan, A. B. & Meyer, H. 2001 Heat transfer and convection onset in a compressible fluid: ^{3}He near the critical point. *Phys. Rev.* E **63**, 056310.

Kogan, A. B., Murphy, D. & Meyer, H. 1999 Onset of Rayleigh-Bénard convection in a very compressible fluid: ^{3}He, near T_c, *Phys. Rev. Lett.* **82**, 4635.

Nitsche, K. & Straub, J. 1987 The critical "hump" of C_v under microgravity, results from D-spacelab experiment "Wärmekapazität". *Proc. 6th European Symp. on Material Sci. under Microgravity Conditions*. ESA SP-256, p. 109.

Onuki, A., Hao, H. & Ferrell, R. A., 1990 Fast adiabatic equilibration in a single-component fluid near the liquid-vapor critical point. *Phys. Rev.* A **41**, 2256.

Paolucci, S. 1982 On the filtering of sound from the Navier-Stokes equations. *Sandia National Lab. Rep.* SAND 82, 8257.

Patankar, S. V. 1980 *Numerical Heat Transfer and Fluid Flow*. Hemisphere.

Poche, P. E., Castaing, B., Chabaud, B. & Hébral, B. 2004 Heat transfer in turbulent Rayleigh-Bénard convection below the ultimate regime. *J. Low Temp. Phys.* **134(5/6)**, 1011.

Siggia, E. D. 1994 High Rayleigh number convection. *Annu. Rev. Fluid. Mech.* **26**, 137.

Straub, J., Eicher, L. & Haupt, A. 1995 Dynamic temperature propagation in a pure fluid near its critical point observed under microgravity during the German Spacelab Mission D-2. *Phys. Rev.* E **51**, 5556.

Verzicco, R. & Camussi, R. 1999 Prandtl number effects in convective turbulence. *J. Fluid Mech.* **383**, 55.

Zappoli, B. 1992 The response of a nearly supercritical pure fluid to a thermal disturbance. *Phys. Fluids* A **4**, 1040.

Zappoli, B., Bailly, D., Garrabos, Y., Le Neindre, B., Guenoun, P. & Beysens, D. 1990 Anomalous heat transport by the piston effect in supercritical fluids under zero gravity. *Phys. Rev.* A **41**, 2264.

Zappoli, B. & Duran-Daubin, A. 1994 Heat and mass transport in a near supercritical fluid. *Phys. Fluids* **6**, 1929.

Zappoli, B., Jounet, A., Amiroudine, S. & Mojtabi, K. 1999 Thermoacoustic heating and cooling in hypercompressible fluids in the presence of a thermal plume. *J. Fluid Mech.* **388**, 389.

Zhong, F. & Meyer, H. 1999 Heat transport in a pure fluid near the critical point: steady state and relaxation dynamics. *J. Low Temp. Phys.* **114**, 231.